Multisite Calibration Tracking for FY-3A MERSI Solar Bands

Ling Sun, Xiuqing Hu, Maohua Guo, and Na Xu

Abstract—The MEdium-Resolution Spectral Imager (MERSI), onboard the second-generation Chinese polar-orbit meteorological satellite FY-3A, is a MODIS-like sensor with 19 solar bands and one thermal infrared band. Although there is a visible onboard calibration device, it can only be used for tracking temporal instrument degradation. The vicarious calibration (VC) campaign at the Dunhuang site, conducted once a year, has been the main postlaunch absolute radiometric calibration method for MERSI in the solar bands. To increase the in-flight calibration frequency, a multisite radiometric calibration tracking method is presented. This method relies on simulated radiation over several stable sites, and a daily calibration updating model is built from long-term trending of calibration coefficient series. The MERSI calibration reference is evaluated against the observations of Aqua MODIS, showing mean relative biases within 5% from 0.4 to 2.1 μm. The short-wave channels of MERSI are found to experience large degradation, particularly the 412-nm band with an annual degradation rate of 9.7%, whereas the red and near-infrared bands are relatively stable with annual degradation rates within $\pm 1\%$. Several approaches have been used to analyze the reliability of MERSI calibration results. A comparison of the calibration slopes shows that the relative biases between the multisite method and the annual Dunhuang VC campaign are below 3.8%. Aqua MODIS is used as a reference to monitor the data quality of the recalibrated MERSI. A double-difference analysis shows that the mean relative biases are almost within 5% over stable deserts, and the synchronous nadir observation analysis also reveals good agreement.

Index Terms—FengYun-3A (FY-3A) MEdium-Resolution Spectral Imager (MERSI), multisite, radiative transfer modeling (RTM), reflective solar bands (RSBs), vicarious calibration (VC).

I. INTRODUCTION

THE FengYun-3 (FY-3) series is the second generation of Chinese polar-orbit meteorological satellites. FY-3A is the first spacecraft launched on May 27, 2008, in a near-sun-synchronous polar orbit with a nominal altitude of 836 km and an equatorial crossing time of 10:30 A.M. (descending southward). MEdium-Resolution Spectral Imager (MERSI) is a keystone payload onboard FY-3A, containing 20 bands cover-ing the spectral range from visible (VIS) to long-wave infrared. The nadir spatial resolution values are 0.25 km (5 bands) and 1 km (15 bands). FY-3A MERSI is capable of making global observations for a broad range of scientific studies of the Earth's systems.

Quantitative remote sensing applications are sensitive to the sensor's radiometric performance, and sensor calibration is a prerequisite. The on-orbit response obviously changes for reflective solar bands (RSBs), particularly short-wave bands with wavelengths less than 500 nm [1], which must be effectively monitored and corrected. Regular and reliable onboard absolute calibration can assure a sensor's radiometric quality with good accuracy and stability. Although an experimental visible onboard calibration (VOC) device exists for MERSI, it can only be used to track the temporal instrument degradation for research purposes because of its nonregular operation and inability to be traced back to a prelaunch standard or SI. Other calibration approaches must be taken to achieve the expected calibration accuracy requirement of 7% for RSBs [2]. There are already many postlaunch calibration and monitoring methodologies in the solar reflective spectral region, including vicarious calibration (VC) based on radiative transfer modeling with input parameters from *in situ* measurements (e.g., [3] and [4]) or other sources (e.g., [5]–[7]); "invariant" target tracking, such as bright desert (e.g., [5], [6], [8], and [9]), glaciers (e.g., [10] and [11]), and deep convective cloud (e.g., [12] and [13]), as well as the moon (e.g., [14] and [15]); and inter-calibration based on a reference sensor or band (e.g., [16] and [17]). China Radiometric Calibration Site (CRCS) for satellite sensor calibration for RSBs is located in Dunhuang Gobi Desert in northwest China. The Dunhuang VC based on synchronous *in situ* measurements has been the baseline calibration approach for Chinese FengYun (FY) series satellites since 2002, and an annual field campaign has been routinely carried out in summer [18]. Although recent studies have demonstrated that CRCS VC has an average accuracy value of approximately 3% for VIS and near-infrared (NIR) window bands with respect to Aqua MODIS [19], the limited frequency of once a year is not enough for effective on-orbit calibration coefficient updating. To increase the postlaunch calibration frequency and monitor the radiometric response change of MERSI, a multisite calibration tracking method based on stable targets and radiative transfer modeling without synchronous *in situ* measurements has been developed at the National Satellite Meteorological Center (NSMC).

The objective of this paper is to present this VC method, including the calibration reference evaluation, long-term sensor response on-orbit change for MERSI, and calibration

L. Sun, X. Hu, and N. Xu are with the National Satellite Meteorological Center, China Meteorological Administration, Beijing 100081, China (e-mail: sunling@ cma.gov.cn).
M. Guo is with the National Satellite Ocean Application Service, State Oceanic Administration, Beijing 100081, China.

TABLE I
MERSI SPECTRAL BAND SPECIFICATIONS

Band	CW (μm)	BW (μm)	IFOV (m)	NEΔρ (%) or NEΔT (K@300K)	Dynamic Range (maximum ρ or T)
1	0.470	0.05	250	0.45	100%
2	0.550	0.05	250	0.4	100%
3	0.650	0.05	250	0.4	100%
4	0.865	0.05	250	0.45	100%
5	11.25	2.5	250	0.4K	330K
6	1.640	0.05	1000	0.08	90%
7	2.130	0.05	1000	0.07	90%
8	0.412	0.02	1000	0.1	80%
9	0.443	0.02	1000	0.1	80%
10	0.490	0.02	1000	0.05	80%
11	0.520	0.02	1000	0.05	80%
12	0.565	0.02	1000	0.05	80%
13	0.650	0.02	1000	0.05	80%
14	0.685	0.02	1000	0.05	80%
15	0.765	0.02	1000	0.05	80%
16	0.865	0.02	1000	0.05	80%
17	0.905	0.02	1000	0.10	90%
18	0.940	0.02	1000	0.10	90%
19	0.980	0.02	1000	0.10	90%
20	1.030	0.02	1000	0.10	90%

CW: Central wavelengths;　　　　BW: Bandwidths;
IFOV: Instantaneous Field of View (nadir).

performance analysis. Following a brief sensor overview in Section II, the methods used in multisite calibration tracking for FY-3A MERSI reflective solar spectral bands as well as the calibration reference uncertainty evaluation with respect to Aqua MODIS, and the calibration result intercomparison are described in Section III. Section IV demonstrates the calibration tracking results and the evaluation of FY-3A MERSI calibration performance, including a comparison of calibration coefficients with those from independent CRCS VC, intercomparison with Aqua MODIS over stable desert targets, and synchronous nadir observation (SNO) targets. Finally, a summary of this paper is provided in Section V.

II. OVERVIEW OF FY-3A MERSI

A. Instrument Description

FY-3A MERSI is a cross-track scanning radiometer using a 45° scan mirror and a derotated K mirror with a scan period of 1.5 s. MERSI makes Earth view observations over a scan angle range of ±55° about nadir. It covers a swath of 2900 km cross track by 10 km (at nadir) along track for each scan with multiple detectors (10 or 40), enabling complete global coverage in one day. It collects data at two nadir spatial resolution values: 250 m (5 bands) and 1000 m (15 bands). It has 20 spectral bands: 19 RSBs with wavelengths from 0.41 to 2.13 μm and one thermal emissive band with a wavelength of 11.25 μm (see Table I). Fig. 1 shows the spectral response functions (SRFs) of FY-3A MERSI RSBs. In total, there are 350 along-track detectors: 40 detectors per band for the channels with a 250-m pixel resolution and 10 detectors per band for the channels with a 1-km pixel resolution. The global moderate-resolution narrow-band observations in 20 spectral bands provide useful data for scientific studies and applications in land, ocean, and atmosphere.

The expected calibration accuracy requirement of RSBs is 7% [2]. MERSI has a VIS/NIR onboard calibration system,

i.e., the visible onboard calibrator for RSBs. It is the first onboard visible calibration experimental device for FY series sensors. It is composed of a 6-cm-diameter integrating sphere with interior lamps and a sunlight import cone, an export beam expanding system with a flat mirror and a parabola to create a collimated beam, and absolute radiance trap detectors (four detectors with the same filter designs as MERSI bands 1–4 with central wavelengths at 470, 550, 650, and 865 nm, and one panchromatic detector with no filter). The export parallel light from the expanding system fills the entrance aperture of MERSI and is viewed for each scan. This device is only used for tracking the temporal instrument degradation for research purposes because of its nonregular operation and inability to be traced back to a prelaunch standard or SI [20].

The VIS and NIR focal plane assemblies (FPAs) utilize p-i-n photovoltaic silicon diodes. The short-wave infrared (SWIR) bands have photovoltaic HgCdTe detectors. The SWIR (bands 6 and 7) FPAs should be cooled to approximately 90 K by a passive radiant cooler. Unfortunately, SWIR bands 6 and 7 are influenced by anomalous electronic gain jumps, possibly induced by electrostatic discharge [19].

B. In-Flight Calibration Updates

The Dunhuang test site, the CRCS for Chinese satellite sensor calibration for RSBs, was selected in 2008 by the Working Group on Calibration and Validation (WGCV) of the Committee on Earth Observation Satellites (CEOS) as one of the instrumented reference sites. It is located on a stable alluvial fan whose surface consists of cemented gravels with some gray or black stones and almost no vegetation. The surface spectral reflectance is temporally stable, and the coefficient of variation (CV), defined as the ratio of standard deviation (Std) over average (Mean), is approximately 3% over the 10 km × 10 km central region. The aerosol loading is low, with an average optical depth of approximately 0.2 at 550 nm, except for during the dusty spring season. The surface reflectance is approximately 15%–30% in the VIS/NIR spectral region, and the surface bidirectional reflectance distribution function (BRDF) was modeled with field measurements in summer 2008 [18].

The CRCS VC based on synchronous *in situ* measurements has been the baseline calibration approach for Chinese FY series satellites since 2002. Field campaigns have been routinely carried out once a year in summer, in which surface spectral reflectance, aerosol optical property, and atmospheric profile are measured. The previous strategy of postlaunch calibration updating for FY sensors is to replace the calibration coefficients with those from the latest CRCS VC campaign when the relative differences between the coefficients of the latest campaign and the previous year exceed 5%.

Although recent studies have shown that CRCS VC has an average accuracy value of approximately 3% for VIS and NIR window bands with respect to Aqua MODIS [19], the limited frequency of once a year is not enough for effective monitoring of sensor response degradation and in-flight calibration coefficient updating. To increase the calibration frequency, CRCS VC is carried out using only synchronous measurements
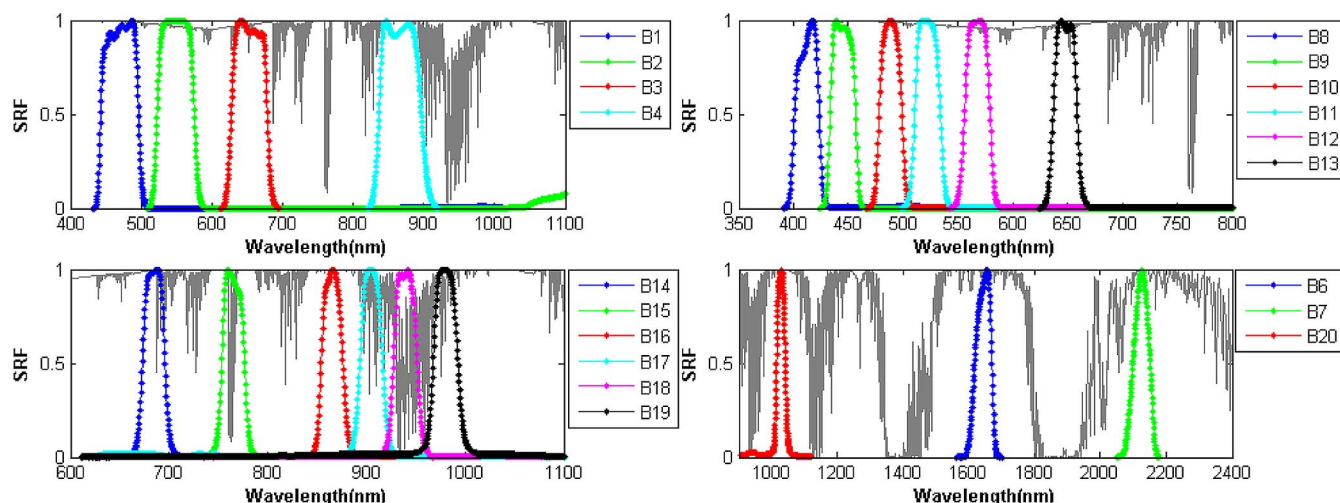
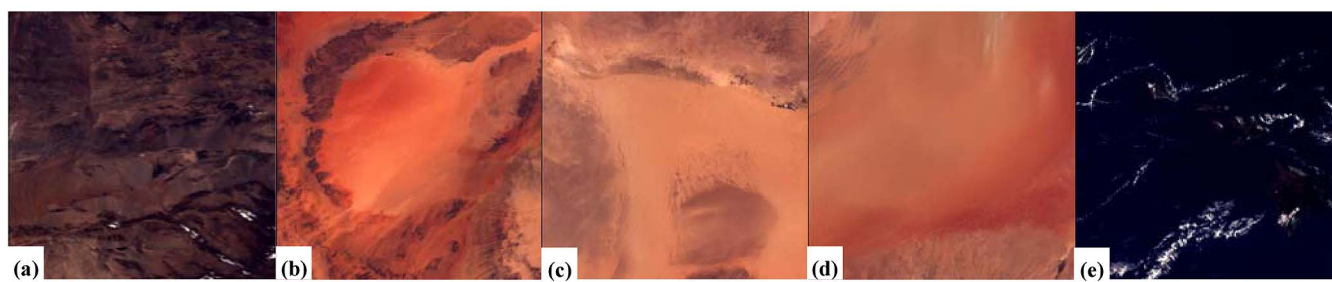Fig. 1. SRFs of FY-3A MERSI RSBs. The gaseous absorption transmittance is shown with the shaded black line.

Fig. 2. True color images from FY-3A MERSI using bands 3, 2, and 1 for RGB. The five target sites are: (a) Dunhuang (40.14° N, 94.32° E); (b) Libya1 (24.42° N, 13.35° E); (c) Libya4 (28.55° N, 23.39° E); (d) Arabia2 (20.13° N, 50.96° E); and (e) Lanai (20.49° N, −157.11° E).

of surface spectral reflectance and aerosol optical depth whenever suitable calibration conditions are met. In addition, many other calibration tracking methods have been used to monitor the radiometric response variation for solar bands, such as stable target long-term trend analysis of deep convective cloud, polar glacier Dome C, and deserts. The multisite radiative transfer modeling method described below is also implemented to fulfill the operational calibration of MERSI RSBs.

III. METHOD

A series of radiometrically stable and bright targets located in the Saharan and Saudi Arabian deserts have been already identified [21] and widely used for solar band calibration, either absolutely or relatively. EUMETSAT has successfully performed the absolute calibration of solar bands using multiple bright desert targets [6]. For FY-3A MERSI, multiple sites with uniform and stable surface properties have been also chosen for radiometric calibration tracking. Three bright desert target sites, namely, Libya1 (24.42° N, 13.35° E), Libya4 (28.55° N, 23.39° E), and Arabia2 (20.13° N, 50.96° E), and one Gobi Desert site, i.e., Dunhuang (40.14° N, 94.32° E), with medium brightness as recommended by CEOS/WGCV, are chosen, as well as a dark ocean site at Lanai (20.49° N, −157.11° E) with Marine Optical BuoY (MOBY) measurements [22]. Fig. 2 shows images of the calibration target sites for MERSI, and their positions are indicated in Fig. 3.
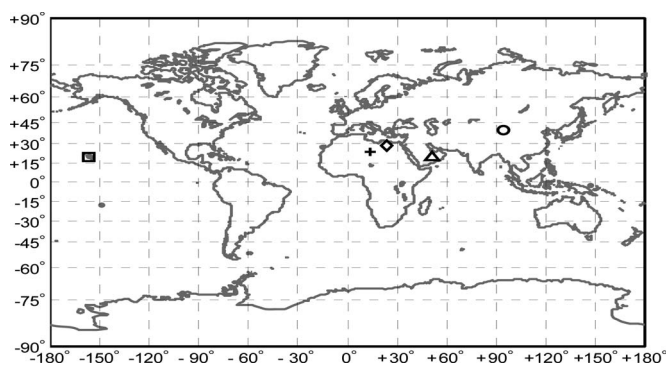

Fig. 3. Locations of the calibration target sites. The Gobi Desert site and three bright desert sites are (indicated with a circle symbol) Dunhuang, (plus symbol) Libya1, (diamond symbol) Libya4, and (triangle symbol) Arabia2. The single sea site is (square symbol) Lanai.

A. Postlaunch Calibration Model

Satellite Data Selection: MERSI 1-km products (aggregated data sets are used for 250-m bands) are mapped using Lambert projection. Pixels in a 3 × 3 box centered around the site center are taken, and the average values are used for calculation according to the following criteria: Spatial uniformity is tested, and data with a large CV value for any bands from 1 to 4 are disregarded; data with solar zenith angle larger than 70° are disregarded for reliable radiative transfer model (RTM) calculation; and a glint angle threshold of 40° is applied to the

Lanai site to avoid sun glint contamination. Residual cloud-contaminated data are discarded if the relative bias between MERSI measured top-of-the-atmosphere (TOA) reflectance and RTM simulation exceeds 30%. Because the sensor response degradation for NIR is small, as described in Section IV, band 4 (865 nm) and Dunhuang VC coefficients from August 2008 [19] are used.

Radiative Transfer Modeling: Spectral radiation is calculated using the vector version of the Second Simulation of a Satellite Signal in the Solar Spectrum radiative transfer code (6SV1) [23] for successfully identified clear-sky targets, accounting for the actual illumination and viewing angles at the acquisition time, the SRFs, and the corresponding surface and atmospheric properties.

The surface bidirectional reflectance of land sites is represented using the MODIS BRDF model [24]. This BRDF model depends on three kernel model parameters that are wavelength dependent. Parameters taken from MCD43C1 products are spectrally interpolated to the central wavelengths of MERSI bands. Water-leaving reflectance is taken from MOBY measurements for the ocean site. A US1962 vertical atmospheric profile is assumed all year long. The desert and maritime aerosol models provided in 6SV1 are assumed for land and ocean sites, respectively. The aerosol optical depth at 550 nm is taken from the MODIS monthly aerosol product (Aqua Deep Blue result for land and Terra result for ocean) [25]. The total column ozone is taken from a monthly mean climate data set that is generated from several years of Total Ozone Mapping Spectrometer observations [26], and the total column water vapor and surface wind speed are taken from a climatology monthly mean from National Center for Environmental Prediction analyzed data [27].

Calibration: TOA reflectance is calculated using the 6SV1 code, and time series consisting of pairs of observed count and simulated reflectance are accumulated for each target site. In general, the calibration coefficient slowly changes with time. Considering that data from multiple sites with different brightness levels could achieve better coverage of sensor dynamic range than from one site and a large amount of data could permit the reduction of calibration errors mainly due to calculated reflectance uncertainties [28], the calibration coefficient is calculated based on the acquisition of data during an accumulation period (e.g., 10 days) and from the five sites with

$$100 \, Ref_i \cos(SolZ)/d^2 = Slope_i(EV_i - SV_i) \quad (1)$$

where Ref_i is the RTM calculated instantaneous TOA reflectance for band i defined as $\pi d^2 Rad/(E_0 \cos(SolZ))$, Rad is the sensor measured radiance of an Earth scene (in $Wm^{-2}sr^{-1}\mu m^{-1}$), E_0 is the extraterrestrial solar irradiance at a distance of one astronomical unit (AU), $SolZ$ is the solar zenith angle, d is the Earth–Sun distance in AU, $Slope$ is the calibration slope, and EV and SV are the digital counts of Earth view observations and space view observations (taken as the radiation zero reference), respectively. In the following, $Ref_i \cos(SolZ)/d^2$ is denoted as the reflectance factor (RefFactor). Fig. 4 shows an example of calibration scatter diagrams

with an accumulation period of ten days for 19 MERSI RSBs, in which three water vapor bands from 17 to 19 are shown just for information. In general, the ocean site plays a small part in obtaining the calibration slopes because of the small amount of data it provides.

Trending: Based on the calibration coefficient series, a linear model is used to describe the long-term varying trend of calibration slopes

$$Slope_i = a_i DSL + b_i \quad (2)$$

where DSL is the number of days since launch, a_i reflects the daily degradation rate of response gain $(1/Slope)$ for band i, and b is the model-estimated initial calibration slope at launch day.

In order to be consistent with other studies, the normalized response for band i is defined as $NResponse_i = b_i/Slope_i$. A linear model for sensor response degradation is also assumed

$$N \, Response_i = c_i DSL + d_i \quad (3)$$

where c and d are degradation model coefficients. Thus, the annual degradation rate of sensor response could be determined through

$$AnnualRate_i = -365 \cdot c_i/d_i. \quad (4)$$

B. Calibration Reference Uncertainty Evaluation

As described in Section III-A, the MERSI calibration reference is the RTM-simulated TOA reflectance. In the above method, the TOA radiation is calculated using almost all parameters from satellite and climatology data sets rather than *in situ* measurements, whose inaccuracies, together with the RTM itself, may affect the TOA radiation accuracy. The objective of this evaluation is to assess the accuracy (bias) and precision (variance) of the MERSI calibration reference against the observations of a well-calibrated sensor, e.g., EOS MODIS. Since the RSB on-orbit performance of Aqua MODIS is better than that of Terra MODIS [1], Aqua MODIS clear-sky observations acquired over the four land sites listed in Section III-A are used as the "TOA truth" to evaluate the TOA radiation simulation performance. This is accomplished by comparing the MODIS measurements with the TOA reflectance simulated by the RTM using the same calculation scheme as MERSI, except for the geometry and band SRF.

The version 5 products of MYD1KM and MYD03 from 2008 to 2009 are obtained from NASA's website. MODIS is usually saturated in bands 11–16 for the Gobi and desert targets, and bands 17, 18, 19, and 26 are affected by water vapor absorption; hence, the evaluation is performed for the first ten bands only. The average values in a 3×3 box centered around the site center are used in the comparison according to the following criteria: Spatial uniformity is tested, and data with a large CV value for any bands from 1 to 5 are disregarded, and if the observed TOA reflectance for band 1 is larger than 0.6, the data are discarded as being nonclear sky.
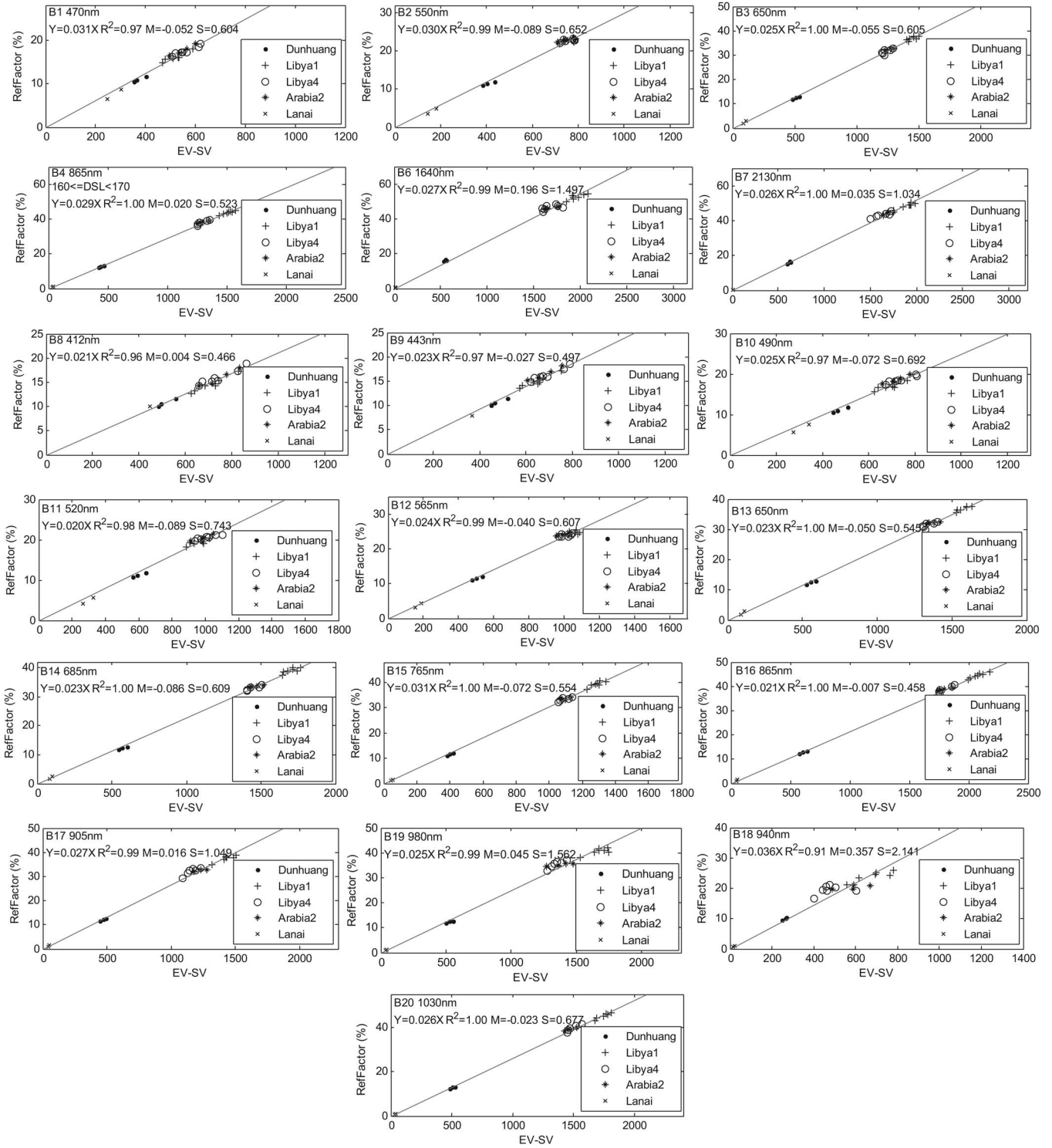
Fig. 4. Typical scatter diagrams of simulated TOA reflectance versus MERSI Earth view digital number with space view subtracted for 19 RSBs. M and S are the mean and the standard deviation between simulated reflectance and the linear calibration line. DSL is the number of days since launch. Between DSL 160 and 170, 23 data points are used.

For each pair of sensor observation and model estimation, the relative bias in percent is defined as

$$PDif = 100 \cdot (Ref^{\text{est}} - Ref^{\text{mea}})/Ref^{\text{mea}} \qquad (5)$$

where Ref^{est} is the RTM-simulated TOA apparent reflectance, and Ref^{mea} is the sensor measurement. Considering the rel-

atively poor performance of RTM at large zenith angles, only data with $SolZ$ less than $70°$ are used in the analysis.

C. Calibration Result Intercomparison

FY-3A MERSI calibration coefficients are updated every day using the calibration updating model given in Section III-A
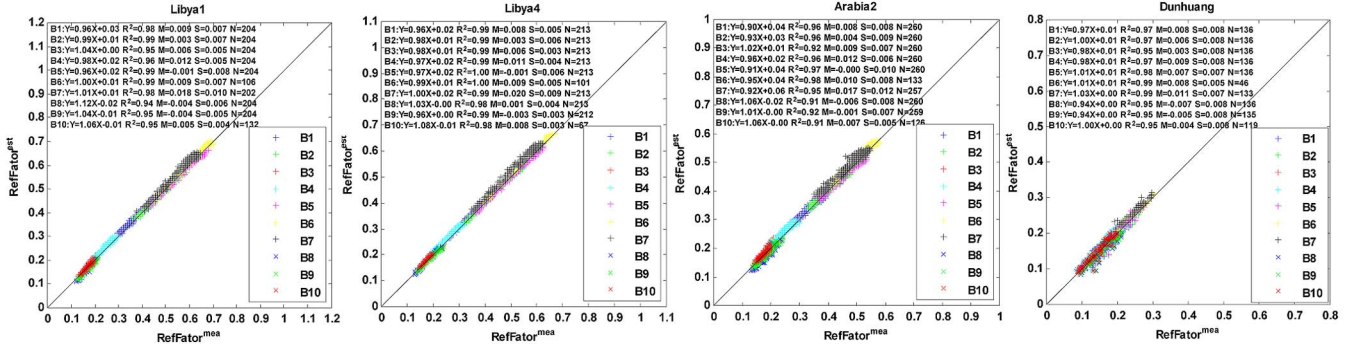
Fig. 5. Scatter diagrams between MODIS measurement and simulated reflectance for Libya1, Libya4, Arabia2, and Dunhuang. Data are acquired from 2008 to 2009. The 1:1 solid line is shown, and the linear fitting statistics (M and S are the mean and the standard deviation of reflectance difference between simulated reflectance and MODIS measurement) are labeled. To increase the data range for plotting, the RefFactor is used here instead of the TOA apparent reflectance.
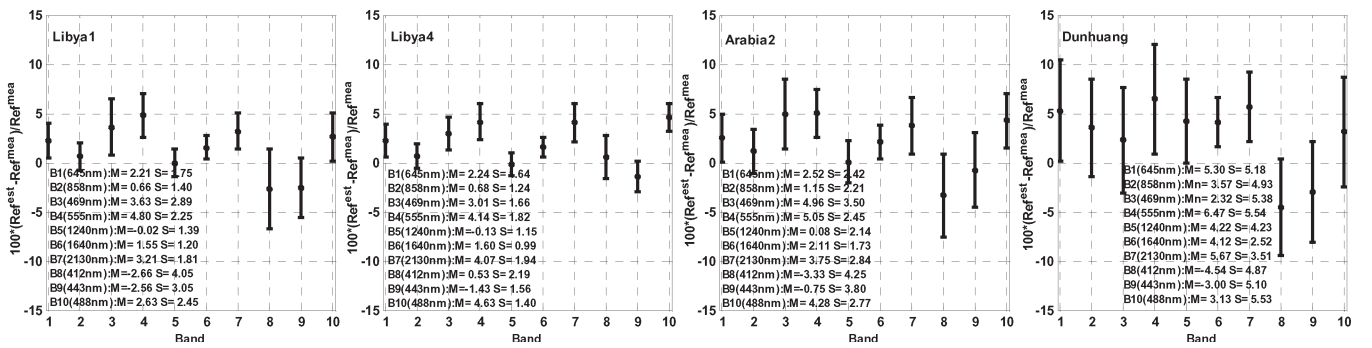

Fig. 6. Mean relative bias in percent between MODIS measured and simulated TOA apparent reflectances for Libya1, Libya4, Arabia2, and Dunhuang with error bar of one standard deviation. The mean (M) and standard deviation (S) values are labeled.

through (2). The postlaunch calibration results of FY-3A MERSI RSBs are analyzed from three aspects.

Since CRCS VC has been carried out once a year with simultaneous *in situ* measurements at Dunhuang, with an average accuracy value of approximately 3% for VIS/NIR window bands with respect to Aqua MODIS [19], the model-estimated calibration slopes are first compared with those from the annual CRCS VC campaigns.

Aqua MODIS is then used as a reference to monitor the data quality of the recalibrated MERSI, in which stable land targets and SNO targets are used. Over uniform and stable ground targets, the calibration difference between FY-3A MERSI and Aqua MODIS can be evaluated using the two expressions [29], [30] in (6) and (7), shown at the bottom of the page, where superscript "Mea" indicates the sensor measurement, superscript "Est" indicates the RTM simulation using the methods described in Section III-A, $\Delta Ratio$ is the ratio of sensor-measured TOA reflectance of MERSI and MODIS after normalization to the RTM simulations, ΔDif is the bias of sensor measurements after normalization to the RTM simulations, and $\Delta Dif/Ref_{\text{MODIS}}^{\text{Mea}}$ is the relative bias of sensor measurements.

These two quantities are derived from closely matched spectral band pairs from FY-3A MERSI and Aqua MODIS acquired on the same clear-sky day. Data over four land sites (Dunhuang, Libya1, Libya4, and Arabia2) from 2008 to 2009 are used. A simple threshold method is applied to screen cloudy data, including the spatial uniformity thresholds described above and a TOA reflectance threshold (0.4 for Dunhuang and 0.6 for other locations for the red band). Data with a solar zenith angle larger than 60° are not included in the analysis. Considering the MODIS saturation phenomenon for some bands and the MERSI anomalous electrical gain jumps in bands 6 and 7, MERSI bands 1–4 and 8–10 are compared with similar MODIS bands.

In addition to the intercomparison over uniform and stable ground targets after normalization to the RTM simulations, recalibrated MERSI TOA reflectance is also cross compared with Aqua MODIS measurements using the SNO method. The version 5 products of MYD1KM and MYD03 are used when the nadir overpass time differences from FY-3A MERSI are within 10 min. Data are mapped using Lambert projection centered at nadir. The following criteria are used in MERSI and MODIS satellite data matching: Angle requirement

$$\Delta Ratio = <Ref_{\text{MERSI}}^{\text{Mea}}/Ref_{\text{MERSI}}^{\text{Est}}>/<Ref_{\text{MODIS}}^{\text{Mea}}/Ref_{\text{MODIS}}^{\text{Est}}> \tag{6}$$

$$\Delta Dif/Ref_{\text{MODIS}}^{\text{Mea}} = \frac{<Ref_{\text{MERSI}}^{\text{Mea}} - Ref_{\text{MERSI}}^{\text{Est}}> - <Ref_{\text{MODIS}}^{\text{Mea}} - Ref_{\text{MODIS}}^{\text{Est}}>}{Ref_{\text{MODIS}}^{\text{Mea}}} \tag{7}$$
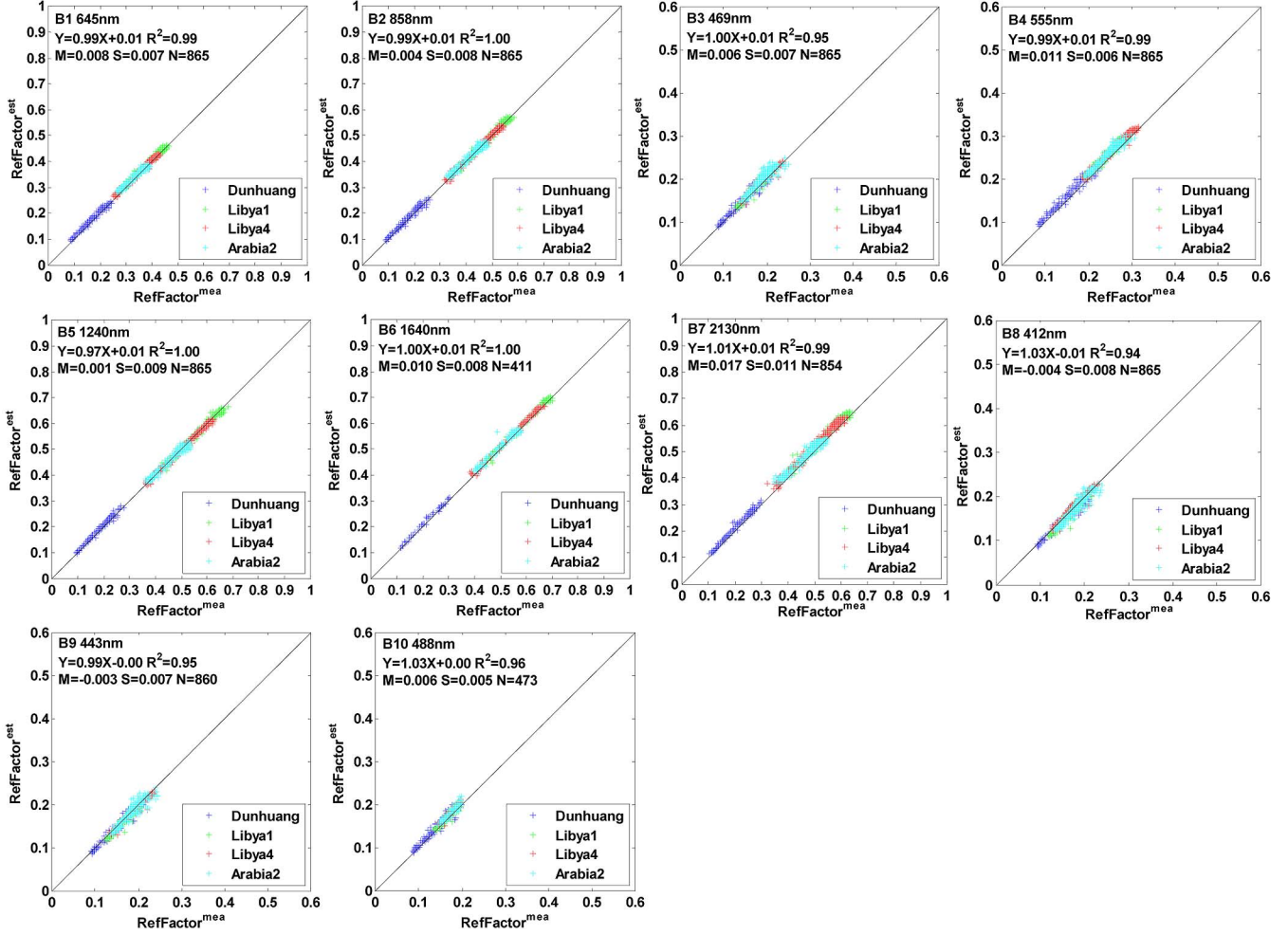
Fig. 7.   Scatter diagrams between MODIS measurement and simulated reflectance with data from all four land sites for bands 1–10. Data are acquired from 2008 to 2009. The 1:1 solid line is shown, and the linear fitting statistics (M and S are the mean and the standard deviation of reflectance difference between simulated reflectance and MODIS measurement) are labeled. To increase the data range for plotting, the RefFactor is used here instead of the TOA apparent reflectance.

of SenZ $< 35°$; $|\cos(\text{SenZ}_{\text{MODIS}})/\cos(\text{SenZ}_{\text{MERSI}}) - 1| <$ 0.01 and $|\cos(\text{SolZ}_{\text{MODIS}})/\cos(\text{SolZ}_{\text{MERSI}}) - 1| <$ 0.01; and space uniformity requirement of CV $< 2\%$ and Std $< 0.1\%$ in each 4×4 box.

IV. RESULTS AND DISCUSSION

A. Calibration Reference Uncertainty

Fig. 5 shows the scatter diagrams of MODIS measured and simulated reflectances for each land site using data from 2008 to 2009. The linear fitting statistics (M and S are the mean and the standard deviation of the difference between the simulated reflectance and the MODIS measurement) are labeled. It should be noted that, to increase the data range for plotting, the RefFactor $(Ref_i \cos(SolZ)/d^2)$ defined in Section III-A is used here instead of the TOA apparent reflectance. Because there are inoperative detectors and saturation phenomena, the CV threshold is used additionally for bands 6, 7, 9, and 10, individually, which results in uneven data amounts. As can be seen, there is a good correlation between simulation and observation, with all R^2 above 0.91. The linear relationships for blue bands, e.g., bands 3, 8, 9, and 10, are not as good
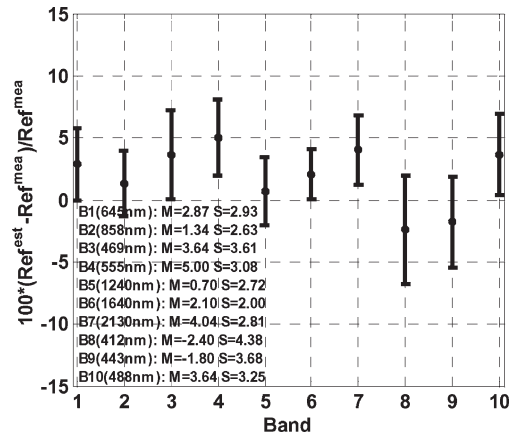
Fig. 8.   Mean relative bias in percent between MODIS measured and simulated TOA apparent reflectances for all four land sites. The error bar represents one standard deviation. The mean and standard deviation values are labeled.

as those for other bands, particularly for the Arabia2 target. These poor results can be explained by the facts that surface reflectance at these sites usually exhibits sharp variations [28], the surface BRDF parameters are obtained from interpolation

Fig. 9. Typical seasonal trends of the monthly mean relative bias in percent between MODIS measured and simulated TOA apparent reflectances using data from all the land sites from 2008 to 2009 for bands 8, 4, 1, 2, 5, and 7. The error bar represents one standard deviation.
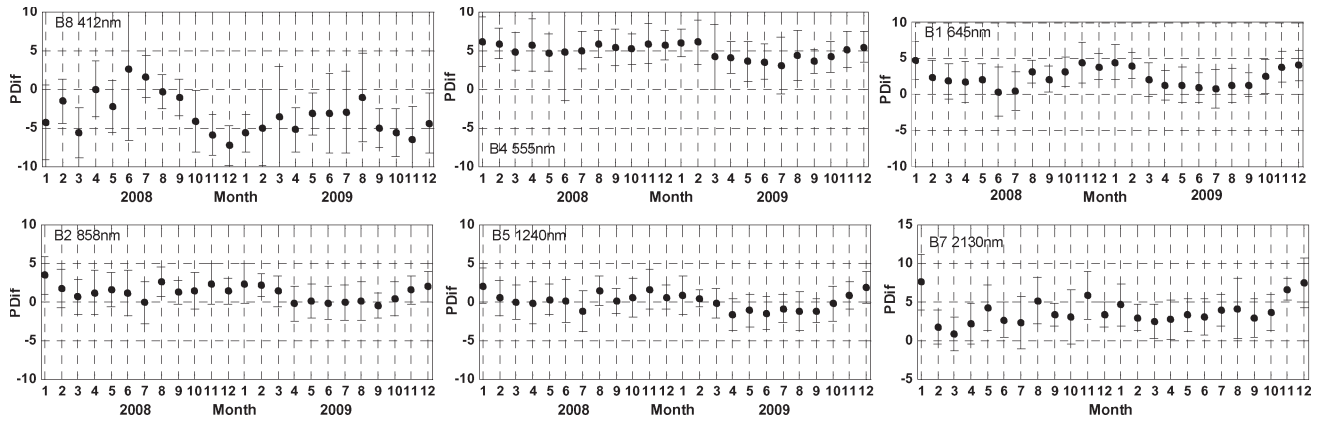
TABLE II
MONTHLY MEAN (M) AND STANDARD DEVIATION (S) OF RELATIVE BIAS IN PERCENT BETWEEN MODIS MEASURED
AND SIMULATED TOA APPARENT REFLECTANCES OVER ALL LAND SITES FROM 2008 TO 2009

Band	Month	1	2	3	4	5	6	7	8	9	10	11	12
1	M	4.95	3.3	2.95	2.13	1.65	1.04	1.56	2.25	2.71	3.63	4.15	4.82
	S	3.56	3.17	3.33	3.04	2.33	2.28	2.12	2.02	2.16	2.46	2.76	3.13
2	M	2.83	1.6	1.91	1.06	0.8	0.3	0.59	1.36	1.22	1.59	1.48	1.87
	S	3.23	3.09	2.94	2.93	2.4	2.23	2	2.18	2.26	2.55	2.6	2.66
3	M	4.39	4.67	4.58	5.31	3.67	3.36	2.82	3.67	3.39	3.07	2.33	3.21
	S	3.12	3.65	4.99	3.9	3.05	4.85	3.39	3.20	2.9	2.91	3.01	2.54
4	M	6.69	5.75	5.44	5.22	3.96	3.54	3.63	4.25	4.68	5.44	5.74	6.55
	S	3.52	3.32	4.02	3.44	2.47	3.16	2.46	2.17	2.26	2.34	2.79	3.08
5	M	1.65	0.56	0.75	-0.1	-0	-0.3	-0.1	0.76	0.67	1.5	1.56	1.7
	S	3.09	2.64	2.74	2.73	2.59	2.3	2.01	2.62	2.55	3.13	2.67	2.65
6	M	2.68	2.21	2.6	1.54	1.74	1.39	1.69	1.63	2.02	2.04	2.7	2.87
	S	2.65	1.51	2.35	1.53	1.71	2.93	1.32	0.93	1.44	1.81	2.13	1.9
7	M	5.12	2.47	2.84	2.47	3.1	3.04	3.98	4.72	4.95	4.99	4.91	5.39
	S	3.66	1.97	3.04	2.16	2.41	1.91	1.91	2.33	2.73	3.15	2.46	3.21
8	M	-3.6	-2.8	-2.5	-0.5	-1.4	-0.5	-1.2	-1.03	-2.2	-3.6	-5.3	-4.7
	S	3.44	4.05	5.36	3.78	3.53	4.99	3.47	3.75	3.77	4.4	4.5	3.58
9	M	-1.8	-1.5	-1.3	0.06	-1.2	-0.9	-1.9	-1.23	-1.8	-2.6	-3.9	-3.1
	S	3.17	3.74	4.98	3.55	2.81	4.92	3.4	3.25	2.9	3.14	3.32	2.66
10	M	4.54	4.12	5.24	7.18	3.46	4.62	3.15	3.15	2.9	3.06	2.68	3.43
	S	2.95	4.01	4.41	4.17	2.43	1.8	3.04	1.66	3.29	2.82	3.1	2.43

for bands 8–10, and the surface reflectance is relatively low for this spectral region.

Fig. 6 shows the mean relative bias in percent between MODIS measured and simulated TOA apparent reflectances for each land site. It reveals that, among the four land sites, the performance is best for Libya4 and relatively poor for Dunhuang. The standard deviation of the relative bias for Dunhuang is obviously larger than for other sites, which can be expected considering the relatively low surface reflectance. Figs. 7 and 8 show the overall scatter diagrams and mean relative bias in percent for all the land sites. It can be seen that, in general, the simulated reflectance tends to be overestimated, except for bands 8 and 9. The mean relative bias is within 5% for the ten bands with central wavelengths from 0.4 to 2.1 μm, and the standard deviation ranges from 2% to 4% with relatively large variances in the blue spectral region.

The temporal behavior is also investigated. It is found that a seasonal trend exists, with one pattern for the blue spectral bands and another pattern for the other bands. The seasonal trend is more obvious for bands 1 (645 nm), 4 (555 nm), and

8 (412 nm). The temporal feature is similar among targets. Fig. 9 shows typical seasonal trends of the monthly mean relative bias in percent between MODIS measured and simulated TOA apparent reflectances using data from all the land sites. Table II lists the monthly mean $PDif$ values averaged over all the land sites from 2008 to 2009. The amount of data for band 10 (488 nm) from March to September is limited; hence, the result for band 10 is given for information only. As shown, the monthly means exhibit variations of approximately 1.5%–4.9% in amplitude, with the minimum at band 6 (1640 nm) and the maximum at band 8 (412 nm). Several factors might be responsible for this temporal trend, including response variation with instrument temperature and inaccuracies of atmospheric and surface parameters. As previous studies have revealed [28], uncertainties in the surface characterization dominate the simulation error. However, the time behavior of MODIS BRDF products is investigated, which shows stable surface property with no noticeable seasonal variation, considering that the temperature dependence of Aqua MODIS's response is well characterized before launch. The most possible reason for this

(a)

Fig. 10.   (Dot symbol) Calibration slope time series for MERSI RSBs (except for SWIR bands 6 and 7 and water vapor absorption bands 17–19) obtained using the multisite calibration method from July 2008 to December 2011. The time variation of the calibration slopes exhibits regular changes that can be fitted with (solid line) a linear model. The dashed line represents one standard deviation of the difference between the calibration slopes and estimations from the fitting model.
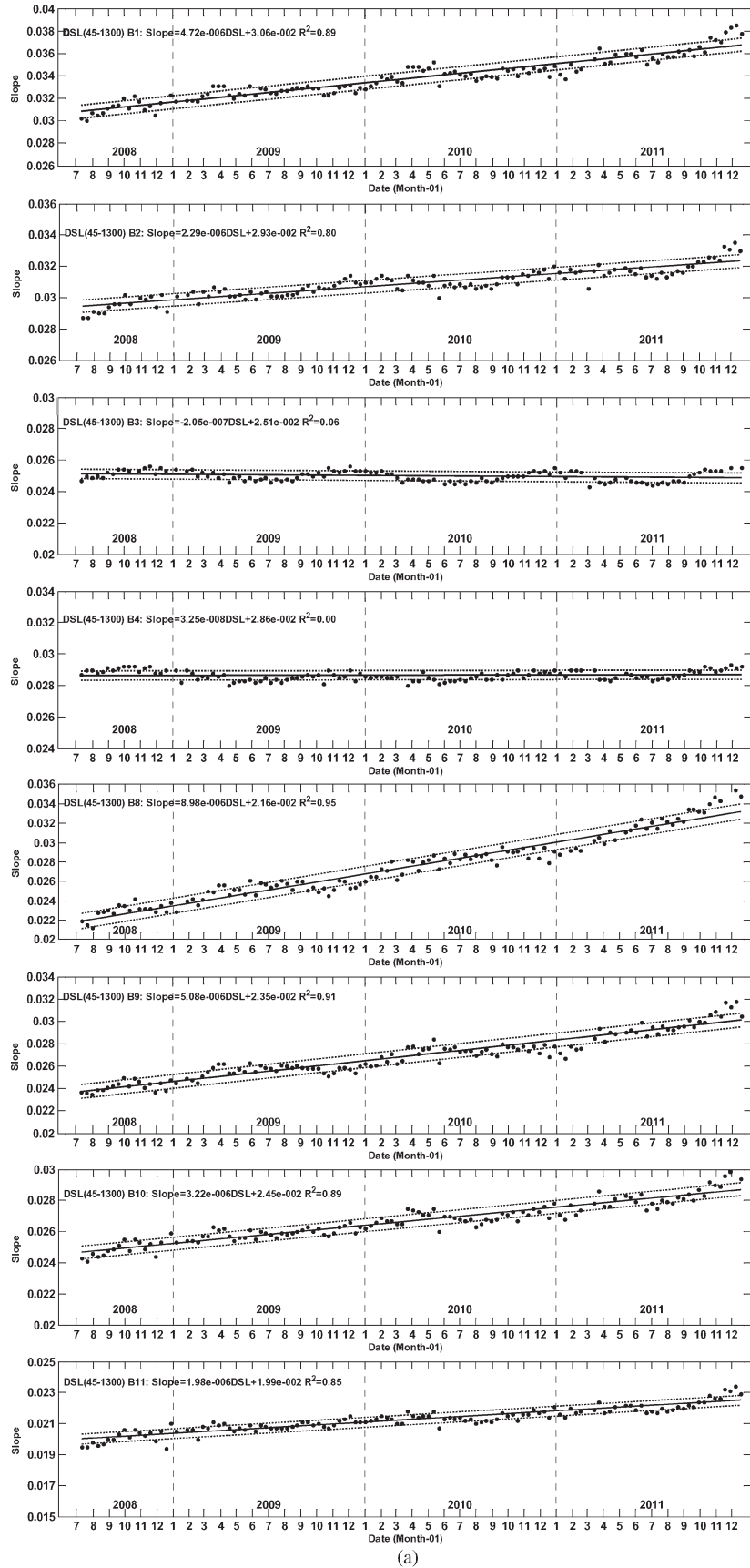
(b)

Fig. 10. (*Continued*). (Dot symbol) Calibration slope time series for MERSI RSBs (except for SWIR bands 6 and 7 and water vapor absorption bands 17–19) obtained using the multisite calibration method from July 2008 to December 2011. The time variation of the calibration slopes exhibits regular changes that can be fitted with (solid line) a linear model. The dashed line represents one standard deviation of the difference between the calibration slopes and estimations from the fitting model.
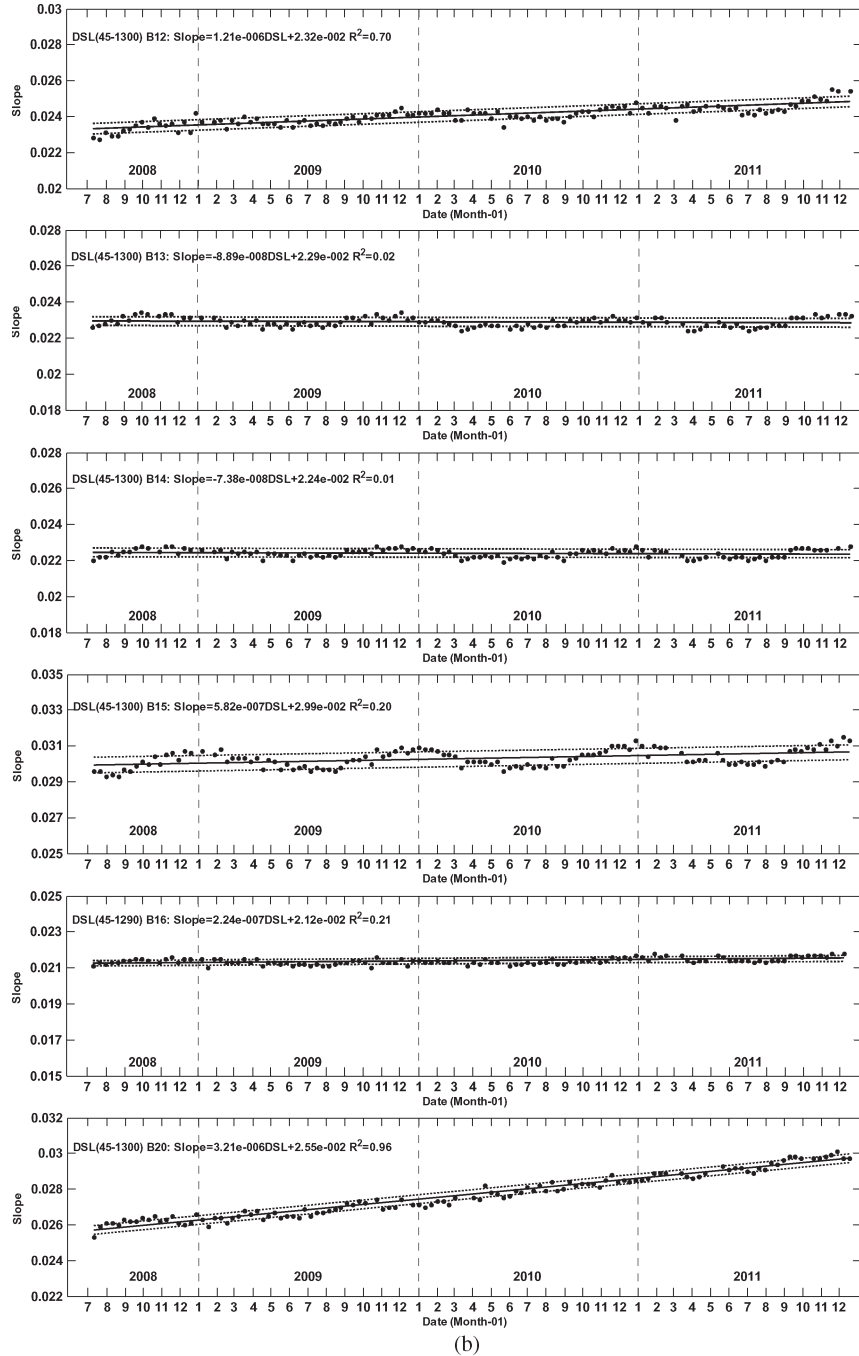
seasonal effect is the inaccuracies of atmospheric parameters, including gas and aerosol. For blue bands, aerosol dominates since gaseous absorption is very weak and aerosol characterization should have a larger impact at shorter wavelengths, whereas gas may be the major reason for other bands.

B. MERSI Calibration Tracking Results

Fig. 10 shows the calibration slope time series for 14 FY-3A MERSI RSBs (excluding three water vapor bands from 17 to 19 and two SWIR bands 6 and 7, affected by anomalous electrical gain jumps), with the linear regression model shown by a solid black line. It can be seen that the calibration coefficients present a linear varying trend with DSL, but a seasonal pattern still exists. For most bands from green to NIR, the calibration coefficients tend to be higher from November to February than from May to August, particularly for the red and NIR spectral regions, e.g., bands 3 (650 nm), 4 (865 nm), 13 (650 nm), 14 (685 nm), 15 (765 nm), and 16 (865 nm). However, the phenomenon tends to be different for blue bands, e.g., bands 1 (470 nm), 8 (412 nm), and 9 (443 nm). As the seasonal features are similar to those discussed in Section IV-A, it could be said

TABLE III
FY-3A MERSI SOLAR BAND CALIBRATION TRACKING ANALYSIS
RESULTS USING THE MULTISITE METHOD

Band	a	b	2σ/Mean (%)	Annual Degradation Rate (%)	Total Degradation Rate (%)
1	4.72E-06	0.0306	3.51	4.64	16.71
2	2.29E-06	0.0293	2.67	2.58	9.27
3	-2.05E-07	0.0251	2.39	-0.30	-1.09
4	3.25E-08	0.0286	2.14	0.04	0.15
8	8.98E-06	0.0216	5.69	9.70	34.91
9	5.08E-06	0.0235	4.43	6.05	21.78
10	3.22E-06	0.0245	3.16	4.06	14.60
11	1.98E-06	0.0199	2.92	3.21	11.54
12	1.21E-06	0.0232	2.42	1.78	6.40
13	-8.89E-08	0.0229	2.14	-0.14	-0.51
14	-7.38E-08	0.0224	2.08	-0.12	-0.44
15	5.82E-07	0.0299	2.77	0.69	2.48
16	2.24E-07	0.0212	1.49	0.38	1.36
20	3.21E-06	0.0255	1.72	3.90	14.04

σ: The standard deviation of difference between calibration
slopes and estimations from the linear regression model.
Mean: The average value of the estimations from the linear model.
Total degradation rate: The degradation rate until the end of 2011.

TABLE IV
RELATIVE BIAS BETWEEN FY-3A MERSI CALIBRATION SLOPES FROM
MULTISITE UPDATING MODEL AND THOSE FROM ANNUAL
CRCS VC AT DUNHUANG FROM 2008 TO 2011

Band	PDif (%) Mean	PDif (%) Std	Band	PDif (%) Mean	PDif (%) Std
1	-1.36	1.98	11	1.99	1.71
2	1.14	1.82	12	-1.30	1.59
3	0.57	0.80	13	0.66	0.59
4	0.35	0.77	14	3.65	0.49
8	-3.62	2.25	15	3.81	1.05
9	-2.82	2.70	16	1.15	0.79
10	2.30	2.49	20	1.80	1.65

PDif=(Slope$_{\text{Multi-sites}}$-Slope$_{\text{CRCS}}$)/Slope$_{\text{CRCS}}$.

that the seasonal pattern is mainly caused by the uncertainty of the calibration method.

Table III lists the statistics of the calibration tracking analysis (bands 6 and 7 and 17–19 are omitted) using data from August 2008 to December 2011, including the parameters (i.e., a and b) and model uncertainty (2σ/mean) for the calibration coefficient updating model (2) and the annual and total (until the end of 2011) response degradation rate. The uncertainty of the calibration coefficient updating model is below 3% except for the blue bands, e.g., bands 1 and 8–10. Polarization sensitivity should also exist for MERSI, but it was not tested before launch. The sensor-received radiation is more polarized at short wave, which may contribute to the relatively large uncertainties of blue bands. It reveals that the response changes are wavelength dependent. Bands with wavelengths less than 600 nm show an obvious degradation, particularly band 8 (412 nm) with an annual degradation rate of approximately 9.7%; bands with wavelengths longer than 900 nm also show a noticeably response decrease, particularly band 20 (1.03 μm) with an annual degradation rate of approximately 3.9%; most red and NIR bands (600–900 nm) are relatively stable with annual degradation rates within ± 1%. Research studies on MODIS have revealed that sensor's SRF, central wavelength, and bandwidth can change during storage prior to launch and during on-orbit operations, and central wavelength shifts change with time and

TABLE V
COMPARISON RESULTS BETWEEN SIMULATED TOA REFLECTANCES
USING SRFS OF MERSI AND MODIS OVER DESERT

MERSI Band (CW)	MODIS Band (CW)	PDif (%) Mean	PDif (%) Std	Ratio Mean	Ratio Std
1 (0.470)	3 (0.469)	0.18	0.20	1.00	0.002
2 (0.550)	4 (0.555)	1.64	0.44	1.02	0.004
3 (0.650)	1 (0.645)	1.47	0.83	1.01	0.008
4 (0.865)	2 (0.858)	-1.37	0.07	0.99	0.001
6 (1.640)	6 (1.640)	-17.26	0.21	0.83	0.002
7 (2.130)	7 (2.130)	25.69	6.08	1.26	0.061
8 (0.412)	8 (0.412)	2.68	0.71	1.03	0.007
9 (0.443)	9 (0.443)	0.71	1.38	1.01	0.014
10 (0.490)	10 (0.488)	-2.12	1.91	0.98	0.019

CW: Center wavelength in μm.
PDif: (Ref$_{\text{SRF\_MERSI}}$- Ref$_{\text{SRF\_MODIS}}$)/Ref$_{\text{SRF\_MODIS}}$.
Ratio: Ref$_{\text{SRF\_MERSI}}$/Ref$_{\text{SRF\_MODIS}}$.

TABLE VI
INTERCOMPARISON RESULTS BETWEEN SENSOR MEASUREMENTS
OF FY-3A MERSI AND AQUA MODIS THROUGH
DOUBLE-DIFFERENCE APPROACH

MERSI Band (CW)	MODIS Band (CW)	$\Delta Dif / Ref_{MODIS}^{Mea}$ (%) Mean	$\Delta Dif / Ref_{MODIS}^{Mea}$ (%) Std	$\Delta Ratio$ Mean	$\Delta Ratio$ Std
1 (0.470)	3 (0.469)	3.37	2.96	1.03	0.03
2 (0.550)	4 (0.555)	5.40	3.63	1.05	0.03
3 (0.650)	1 (0.645)	3.42	3.34	1.03	0.03
4 (0.865)	2 (0.858)	1.09	2.95	1.01	0.03
8 (0.412)	8 (0.412)	-2.95	3.78	0.97	0.04
9 (0.443)	9 (0.443)	-2.39	2.76	0.98	0.03
10 (0.490)	10 (0.488)	3.84	3.47	1.04	0.03

instrument temperature variations [31], particularly the band at 412 nm. Unfortunately, there is no onboard spectral monitoring device for MERSI; hence, the influence of spectral change has not been determined.

C. Intercomparison With CRCS VC and MODIS

FY-3A MERSI calibration slopes estimated by the postlaunch calibration model are compared with those from the annual CRCS VC campaign from 2008 to 2011. Table IV lists the relative bias between them. It shows that the mean relative bias between estimated coefficients through (2) and CRCS VC with *in situ* measurements is below 3.8%.

For the intercomparison between MERSI and MODIS, the difference of viewing geometry and SRF should be considered. When using the double-difference approach over stable targets, the effects of viewing and solar angle differences could be canceled out after normalization to the RTM simulations. However, for high-quality radiometric calibration intercomparison, the impact due to spectral response differences must be also evaluated. Spectral TOA radiation over desert has been simulated under various geometries and convolved with the SRFs of FY-3A MERSI and Aqua MODIS. Table V lists the difference statistics between simulated TOA reflectances using the SRFs of MERSI and MODIS. It is found that the relative bias caused by sensor SRFs is very high for SWIR bands 6 and 7 and is almost below 2% for other bands, except for MERSI bands 8 and 10. Linear models ($R^2 = 1.0$) are thus obtained to be applied in the SRF transformation between MODIS and MERSI. Fig. 11 displays the normalized frequency histograms of $\Delta Dif / Ref_{\text{MODIS}}^{Mea}$ for MERSI bands 1–4 and 8–10. As shown, the difference seems
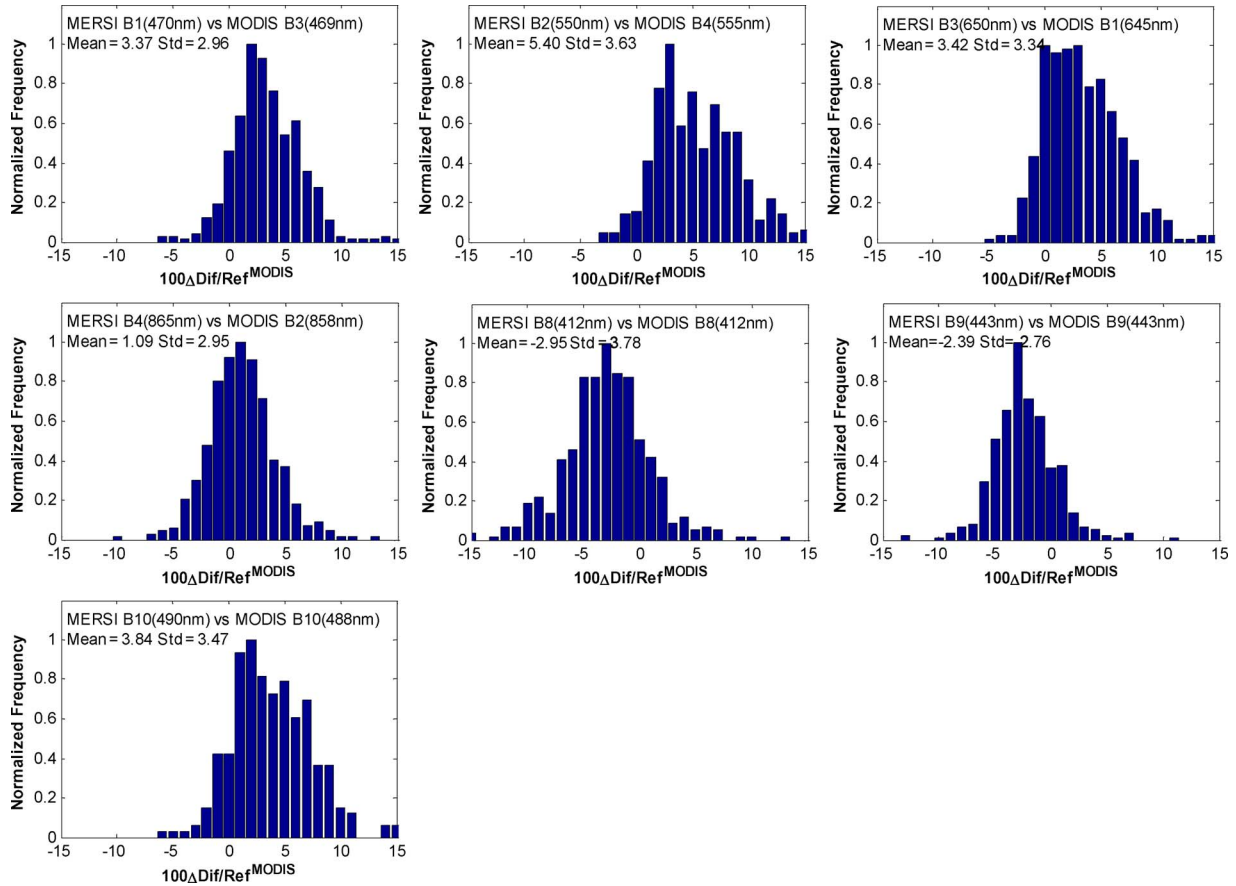
Fig. 11.   Normalized frequency histograms of relative bias between MERSI and MODIS measurements through a double-difference approach.
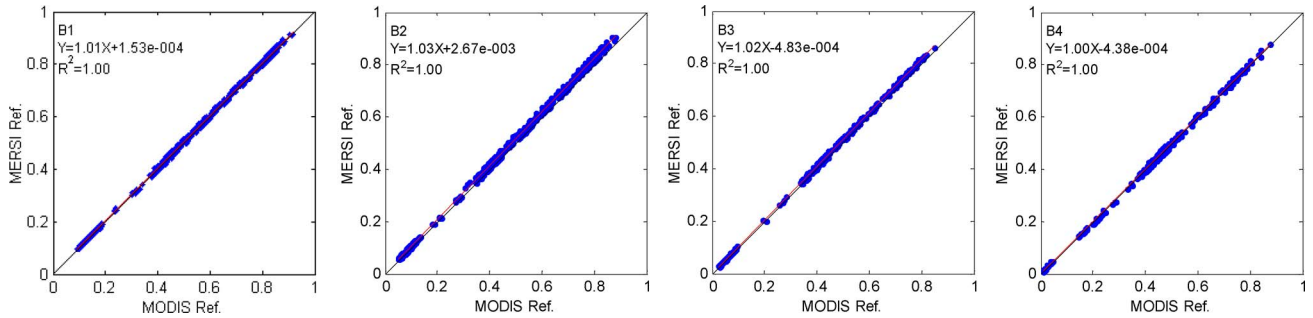

Fig. 12.   TOA apparent reflectance scatter plot between recalibrated FY-3A MERSI and Aqua MODIS in August 2010 for MERSI bands 1, 2, 3, and 4.

like a normal distribution. Table VI lists the intercomparison statistics for matched band pairs through the double-difference approach. It shows that MERSI measurements are higher than MODIS measurements, except for bands 8 and 9. The mean values of $\Delta Dif/Ref_{\mathrm{MODIS}}^{Mea}$ are almost within 5%, and the mean values of $\Delta Ratio$ range from 0.97 to 1.05.

Simulations over different surface types show that the influences of different SRFs are relatively small for the first four bands (results are not shown here). The SNO cross comparison is then performed for MERSI bands 1–4 only. Fig. 12 shows the TOA apparent reflectance scatter plot derived from FY-3A MERSI and Aqua MODIS in August 2010. Good consistency is shown, with fine linear relationships with R^2 nearly 1.0 and slopes from 1 to 1.03. The bias statistics between MERSI and MODIS are listed in Table VII. It shows that the mean

TABLE VII
SNO COMPARISON RESULTS BETWEEN RECALIBRATED FY-3A
MERSI AND AQUA MODIS IN AUGUST 2010

MERSI	MODIS	PDif (%)		Ratio	
Band (CW)	Band (CW)	Mean	Std	Mean	Std
1 (0.470)	3 (0.469)	0.67	1.85	1.01	0.02
2 (0.550)	4 (0.555)	6.75	3.94	1.07	0.04
3 (0.650)	1 (0.645)	0.54	2.98	1.01	0.03
4 (0.865)	2 (0.858)	-0.76	4.41	0.99	0.04

PDif: $(Ref_{\mathrm{MERSI}}$-$Ref_{\mathrm{MODIS}})/Ref_{\mathrm{MODIS}}$.
Ratio: $Ref_{\mathrm{MERSI}}/Ref_{\mathrm{MODIS}}$.

relative biases are 0.67%, 6.75%, 0.54%, and -0.76% for MERSI bands 1 (470 nm), 2 (550 nm), 3 (650 nm), and 4 (865 nm), respectively. Band 2 of MERSI has an obvious out-of-band response at wavelength longer than 1 μm [19], which may contribute to the large difference. It should be noted

that, without correction for SRF difference, the bias statistics are given here for information rather than the evaluation of calibration accuracy.

V. SUMMARY AND CONCLUSION

The experimental VOC device in MERSI cannot be used for reliable absolute calibration in solar bands. Former postlaunch calibration updating has depended on the annual CRCS VC field campaign. However, the limited frequency of once a year is not enough for effective monitoring of sensor response degradation and in-flight calibration coefficient updating. A multisite radiometric calibration method has been developed and presented to increase the calibration frequency. Radiative transfer simulated radiation over several stable targets is used as the calibration reference, and a daily calibration updating model is built from long-term trending of calibration coefficient series.

The MERSI calibration reference is evaluated against the observations of Aqua MODIS, with a mean relative bias within 5% for the first ten bands with central wavelengths from 0.4 to 2.1 μm and a standard deviation ranging from 2% to 4%. Seasonal patterns exist for which the inaccuracy in characterization of the atmospheric property seems to be the main cause. It is found that the MERSI response changes are wavelength dependent. Bands with wavelengths less than 600 nm show obvious degradation, particularly band 8 (412 nm) with an annual degradation rate of approximately 9.7%; bands with wavelengths longer than 900 nm also show a noticeable response decrease; most red and NIR bands (600–900 nm) are relatively stable with annual degradation rates within $\pm 1\%$. Several approaches have been used to analyze the reliability of the calibration results for MERSI. Calibration slopes of FY-3A MERSI are first compared with CRCS VC results, showing the mean relative biases below 3.8% for most bands. A double-difference approach is used to evaluate the calibration difference against Aqua MODIS after normalization to the RTM simulations, showing mean relative biases that are almost within 5% and mean ratios ranging from 0.97 to 1.05 over stable deserts. In addition, the SNO approach is applied, which also reveals good agreement.

In general, this paper is an attempt to assure frequent and stable calibration updating for MERSI RSBs. Most of the validation results presented here indicate that this method is acceptable for fulfilling the MERSI calibration accuracy requirement of 7%. More targets are planned to be included in the calibration process, and more validation and analysis efforts are also needed for further evaluation of the MERSI calibration, including polarization, SRFs, temperature correction, etc.

REFERENCES

[1] X. Xiong, J. Sun, X. Xie, W. L. Barnes, and V. V. Salomonson, "On-orbit calibration and performance of Aqua MODIS reflective solar bands," *IEEE Trans. Geosci. Remote Sens.*, vol. 48, no. 1, pp. 535–546, Jan. 2010.

[2] L. Sun, X. Hu, M. Guo, J. Zhu, S. Li, and L. Ding, "An introduction to FY-3/MERSI, ocean colour algorithm, product and applica-

[3] Y. Zhang, K. Qiu, and X. Hu, "Vicarious radiometric calibration of satellite FY-1D sensors at visible and near infrared channels," *Acta Meteorol. Sin.*, vol. 18, no. 4, pp. 505–516, Jul. 2004.

[4] S. F. Biggar, K. J. Thome, and W. Wisniewski, "Vicarious radiometric calibration of EO-1 sensors by reference to high-reflectance ground targets," *IEEE Trans. Geosci. Remote Sens.*, vol. 41, no. 6, pp. 1174–1179, Jun. 2003.

[5] Y. J. Kaufman and B. N. Holben, "Calibration of the AVHRR visible and near-IR bands by atmospheric scattering, ocean glint and desert reflection," *Int. J. Remote Sen.*, vol. 14, no. 1, pp. 21–52, Jan. 1993.

[6] Y. M. Govaerts, M. Clerici, and N. Clerbaux, "Operational calibration of the Meteosat radiometer VIS band," *IEEE Trans. Geosci. Remote Sens.*, vol. 42, no. 9, pp. 1900–1914, Sep. 2004.

[7] A. Okuyama, T. Hashimoto, R. Nakayama, Y. Tahara, T. Kurino, H. Takenaka, S. Fukuda, T. Y. Nakajima, A. Higurashi, M. Sekiguchi, T. Takamura, and T. Nakajima, "Geostationary imager visible channel recalibration," in *Proc. EUMETSAT Meteorol. Satellite Conf.*, Bath, U.K., Sep. 2009, [CD-ROM].

[8] C. R. N. Rao and J. Chen, "Revised post-launch calibration of the visible and near-infrared channels of the Advanced Very High Resolution Radiometer (AVHRR) on the NOAA-14 spacecraft," *Int. J. Remote Sen.*, vol. 20, no. 18, pp. 3485–3491, Dec. 1999.

[9] X. Wu, J. T. Sullivan, and A. K. Heidinger, "Operational calibration of the Advanced Very High Resolution Radiometer (AVHRR) visible and near-infrared channels," *Can. J. Remote Sens.*, vol. 36, no. 5, pp. 602–616, Oct. 2010.

[10] N. G. Loeb, "In-flight calibration of NOAA AVHRR visible and near-IR bands over Greenland and Antarctica," *Int. J. Remote Sen.*, vol. 18, no. 3, pp. 477–490, Feb. 1997.

[11] W. R. Tahnk and J. A. Coakley, "Updated calibration coefficients for NOAA-14 AVHRR channels 1 and 2," *Int. J. Remote Sen.*, vol. 22, no. 15, pp. 3053–3057, Oct. 2001.

[12] D. R. Doelling, G. Hong, D. Morstad, R. Bhatt, A. Gopalan, and X. Xiong, "The characterization of deep convective cloud albedo as a calibration target using MODIS reflectances," in *Proc. SPIE*, Oct. 2010, vol. 7862, p. 78 620I.

[13] B.-J. Sohn, S.-H. Ham, and P. Yang, "Possibility of the visible-channel calibration using deep convective clouds overshooting the TTL," *J. Appl. Meteorol. Climatol.*, vol. 48, no. 11, pp. 2271–2283, Nov. 2009.

[14] W. Barnes, X. Xiong, R. Eplee, J. Sun, and C.-H. Lyu, "Use of the Moon for calibration and characterization of MODIS, SeaWiFS, and VIRS," in *Earth Science Satellite Remote Sensing*, J. J. Qu, W. Gao, M. Kafatos, R. E. Murphy, and V. V. Salomonson, Eds. New York: Springer-Verlag, 2006, pp. 98–119.

[15] C. Cao, E. Vermote, and X. Xiong, "Using AVHRR lunar observations for NDVI long-term change detection," *J. Geophys. Res.*, vol. 114, pp. D20105-1–D20105-9, Oct. 2009.

[16] A. K. Heidinger, C. Cao, and J. T. Sullivan, "Using Moderate Resolution Imaging Spectrometer (MODIS) to calibrate Advanced Very High Resolution Radiometer reflectance channels," *J. Geophys. Res.*, vol. 107, no. D23, p. 4702, Dec. 2002.

[17] J. Liu, Z. Li, Y. L. Qiao, Y. J. Liu, and Y. X. Zhang, "A new method for cross-calibration of two satellite sensors," *Int. J. Remote Sen.*, vol. 25, no. 23, pp. 5267–5281, Dec. 2004.

[18] X. Hu, J. Liu, L. Sun, Z. Rong, Y. Li, Y. Zhang, Z. Zheng, R. Wu, L. Zhang, and X. Gu, "Characterization of CRCS Dunhuang test site and vicarious calibration utilization for Fengyun (FY) series sensors," *Can. J. Remote Sens.*, vol. 36, no. 5, pp. 566–582, Oct. 2010.

[19] L. Sun, M. Guo, N. Xu, L. Zhang, J. Liu, X. Hu, Y. Li, and Z. Rong, "On-orbit response variation analysis of FY-3 MERSI reflective solar bands based on Dunhuang site calibration," *Spectrosc. Spectral Anal.*, vol. 32, no. 7, pp. 1869–1877, 2012.

[20] X. Hu, L. Sun, J. Liu, L. Ding, X. Wang, Y. Li, Y. Zhang, N. Xu, and L. Chen, "Calibration for the solar reflective bands of Medium Resolution Spectral Imager onboard FY-3A," *IEEE Trans. Geosci. Remote Sens.*, vol. 50, no. 12, pp. 4915–4928, Dec. 2012.

[21] H. Cosnefroy, M. Leroy, and X. Briottet, "Selection and characterization of Saharan and Arabian desert sites for the calibration of optical satellite sensors," *Remote Sens. Environ.*, vol. 58, no. 1, pp. 101–114, Oct. 1996.

[22] D. K. Clark, H. R. Gordon, K. J. Voss, Y. Ge, W. Broenkow, and C. Trees, "Validation of atmospheric correction over the oceans," *J. Geophys. Res.*, vol. 102, no. D14, pp. 17 209–17 217, Jul. 1997.

[23] S. Y. Kotchenova, E. F. Vermote, R. Matarrese, and F. J. Klemm, "Validation of a vector version of the 6S radiative transfer code for atmospheric

correction of satellite data. Part I: Path radiance," *Appl. Opt.*, vol. 45, no. 26, pp. 6762–6774, Sep. 2006.

[24] C. B. Schaaf, F. Gao, A. H. Strahler, W. Lucht, X. Li, T. Tsang, N. C. Strugnell, X. Zhang, Y. Jin, J. P. Muller, P. Lewis, M. Barnsley, P. Hobson, M. Disney, G. Roberts, M. Dunderdale, C. Doll, R. P. d'Entremont, N. Hu, S. Liang, J. L. Privette, and D. Roy, "First operational BRDF, albedo nadir reflectance products from MODIS," *Remote Sens. Environ.*, vol. 83, no. 1–4, pp. 135–148, Nov. 2002.

[25] L. A. Remer, D. Tanre, Y. J. Kaufman, S. Mattoo, D. Chu, J. Martins, R. Li, C. Ichoku, R. Levy, R. Kleidman, T. Eck, E. Vermote, and B. Holben, "The MODIS aerosol algorithm, products and validation," *J. Atmos. Sci.*, vol. 62, no. 4, pp. 947–973, Apr. 2005.

[26] R. McPeters, M. Kroon, G. Labow, E. Brinksma, D. Balis, I. Petropavlovskikh, J. P. Veefkind, P. K. Bhartia, and P. F. Levelt, "Validation of the Aura Ozone Monitoring Instrument total column ozone product," *J. Geophys. Res.*, vol. 113, no. D15, pp. D15S14-1–D15S14-9, May 2008.

[27] E. Kalnay, M. Kanamitsu, R. Kistler, W. Collins, D. Deaven, L. Gandin, M. Iredell, S. Saha, G. White, J. Woollen, Y. Zhu, M. Chelliah, W. Ebisuzaki, W. Higgins, J. Janowiak, K. C. Mo, C. Ropelewski, J. Wang, A. Leetmaa, R. Reynolds, R. Jenne, and D. Joseph, "The NCEP/NCAR 40-year reanalysis project," *Bull. Amer. Meteorol. Soc.*, vol. 77, no. 3, pp. 437–472, Mar 1996.

[28] Y. M. Govaerts and M. Clerici, "Evaluation of radiative transfer simulations over bright desert calibration sites," *IEEE Trans. Geosci. Remote Sens.*, vol. 42, no. 1, pp. 176–187, Jan. 2004.

[29] X. Xiong, A. Wu, B. Wenny, J. Choi, and A. Angal, "Progress and lessons from MODIS calibration intercomparison using ground test sites," *Can. J. Remote Sens.*, vol. 36, no. 5, pp. 540–552, 2010.

[30] D. C. Tobin, H. E. Revercomb, R. O. Knuteson, F. A. Best, W. L. Smith, N. N. Ciganovich, R. G. Dedecker, S. Dutcher, S. D. Ellington, R. K. Garcia, H. B. Howell, D. D. LaPorte, S. A. Mango, T. S. Pagano, J. K. Taylor, P. van Delst, K. H. Vinson, and M. W. Werner, "Radiometric and spectral validation of Atmospheric Infrared Sounder observations with the aircraft-based Scanning High-Resolution Interferometer Sounder," *J. Geophys. Res.*, vol. 111, pp. D09S02-1–D09S02-14, Mar. 2006.

[31] X. Xiong, N. Che, and W. L. Barnes, "Terra MODIS on-orbit spectral characterization and performance," *IEEE Trans. Geosci. Remote Sens.*, vol. 44, no. 8, pp. 2198–2206, Aug. 2006.

Xiuqing Hu received the B.S. degree in atmospheric science from Nanjing University, Nanjing, China, in 1996, the M.S. degree in cartography and geographical information system from Beijing Normal University, Beijing, China, in 2004, and the Ph.D. degree in quantitative remote sensing science from the Institute of Remote Sensing Application, Chinese Academy of Sciences, Beijing, in 2012.

He was a Research Assistant in the National Satellite Meteorological Center, China Meteorological Administration (NSMC/CMA), Beijing, from 1996 to 2004 and became an Associate Professor and the Chief of the CAL/VAL Branch, Satellite Meteorological Institute, NSMC/CMA, in 2004. He has been a Professor of engineering since 2010 and has been the Instrument Scientist of MERSI onboard FY-3 since 2006. He is currently a Visiting Scientist and also a Contractor in NOAA/NESDIS/STAR as a Remote Sensing Senior Scientist with Earth Resources Technology Inc. His research interests include calibration and validation for optical sensors, the retrieval algorithm of aerosol/dust and water vapor, and the climate data record from environment satellite.

Prof. Hu is a member of WMO Sand and Dust Storm Warning Advisory and Assessment System (SDS-WAS) Regional Steering Group and a member of GSICS Research Working Group.

Maohua Guo received the B.S. degree in computer application from North China University of Technology, Beijing, China, in 2000.

He has been an Engineer with the National Satellite Ocean Application Service, State Oceanic Administration, Beijing, since 2005. He has been working on the construction of a remote sensing application system, particularly for the Chinese HaiYang series sensors. His research interests include remote sensing of sea surface temperature and algal bloom.

Ling Sun received the M.S. degree in signal and information processing from Qingdao Ocean University, Qingdao, China, in 2002 and the Ph.D. degree in physical oceanology from the Chinese Academy of Sciences, Qingdao, in 2005.

She became an Associate Professor with the National Satellite Meteorological Center, China Meteorological Administration (NSMC/CMA), Beijing, China, in 2008, and the Agency Chief of the CAL/VAL Branch, Satellite Meteorological Institute, NSMC/CMA, in 2011. She has been the Product Scientist of FY-3 project for ocean color and aerosol over ocean since 2006. She is currently working on the optical instrument calibration and validation at visible bands. Her research interests include calibration and validation for optical sensors and remote sensing of ocean color and aerosol.

Na Xu received the Ph.D. degree in atmospheric physics and environment from the Chinese Academy of Sciences, Beijing, China, in 2010. Her thesis was on the modification and application of an atmospheric radiative transfer model.

She is currently a Research Assistant with the National Satellite Meteorological Center, China Meteorological Administration, Beijing. She is working on the vicarious calibration of FengYun satellite instruments.